Experiments in Fluids (2019) 60:112
https://doi.org/10.1007/s00348-019-2758-6

RESEARCH ARTICLE

Comparison of wall shear stress estimates obtained by laser Doppler velocimetry, magnetic resonance imaging and numerical simulations

Andreas Bauer[1] · Sebastian Wegt[1] · Maximilian Bopp[1] · Suad Jakirlic[1] · Cameron Tropea[1] · Axel Joachim Krafft[2] · Nina Shokina[2] · Jürgen Hennig[2] · Gabriel Teschner[3] · Herbert Egger[3]

Received: 2 January 2019 / Revised: 4 June 2019 / Accepted: 4 June 2019 / Published online: 18 June 2019

Abstract

The wall shear stress (WSS) acting on human vessel walls may play an important role in the emergence of cardiovascular diseases such as aneurysms or arteriosclerosis and is of great interest in the medical context. Magnetic resonance velocimetry (MRV) is a possible method to measure this quantity; however, the most appropriate procedure for the measurement and the achievable accuracy are open and controversial topics. In this study, we examine the accuracy of WSS estimates obtained from in vitro MRV measurements by comparing results with those obtained using laser Doppler velocimetry, with numerical simulations and for some cases with analytic solutions, all for flow conditions typical of the human aorta. The comparisons indicate that under certain conditions, WSS measurements from MRV are feasible and reliable. This work forms the basis for a systematic assessment of WSS estimators using newly developed post-processing algorithms and is considered a first step to improving the in vivo measurements of wall shear stress.

Graphic abstract

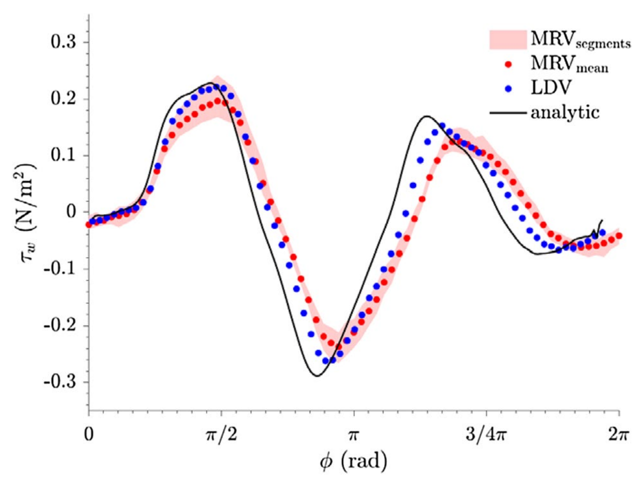

1 Introduction

An ongoing interest in medicine is to predict and prevent diseases of the human circulatory system. One potential indicator and trigger mechanism, which may lead to transformations of the vessel walls and subsequently to cardiovascular diseases, is altered wall shear stress (WSS), which arises due to friction between the blood flow and the vessel wall. The influence of WSS on cardiovascular diseases has

✉ Cameron Tropea
ctropea@sla.tu-darmstadt.de

Extended author information available on the last page of the article been studied extensively and controversially in the literature (Bürk et al. 2012; Callaghan and Grieve 2018; van Ooij et al. 2017; Peiffer et al. 2013; Piatti et al. 2017; Rizk et al. 2019). There is a wide variety of malfunctions of the circulatory system which are potentially associated with altered WSS.

One severe kind of malfunction is the emergence of enlargements of the vessel diameter, so-called aneurysms. Great interest exists to develop techniques which can predict the growth and risk of rupture of such aneurysms and develop early treatments based on this knowledge (Xiang et al. 2011). The results from Harloff et al. (2010) indicate that the location and occurrence of plaque is highly correlated with the WSS as well as occurrence of stenosis in arteries (Siedek et al. 2018). Farag et al. (2019) showed that the transcatheter aortic valve replacement considerably increases the blood flow velocity and thus the WSS in the ascending aorta.

The difficulty from a technical point of view is how the wall shear stress can be measured in vivo. Several techniques exist and an overview can be found in Vennemann et al. (2007), the most promising results being obtained with magnetic resonance velocimetry (MRV). In this context, clinical magnetic resonance imaging (MRI) scanners can be used to measure the velocities of moving protons bound in water molecules and therefore the blood velocity. The wall shear stress can be evaluated by calculating the velocity gradient in the wall-normal direction at the wall. Today, the most common MRV method is phase contrast magnetic resonance imaging (PC-MRI) which has been used for in vivo as well as in vitro applications (Amili et al. 2018; Rizk et al. 2019; Szajer and Ho-Shon 2018). In recent years, considerable progress has been made regarding time-resolved three-dimensional MRV measurements including velocity encoding in all three spatial directions. This technique is typically referred to as 4D flow MRI (Markl et al. 2012).

The main limitation of MRV measurements is the low spatial resolution, typically in the order of 1 mm for scans in the human body. An increase in spatial resolution necessitates longer measurement times to provide sufficient signal to noise levels, which, however, is not practical for data acquisition in patients. The low spatial resolution generally results in an underestimation of the WSS, yielding errors of up to 40% (Petersson et al. 2012). To improve the calculation of the wall shear stress, several techniques exist which focus primarily on the post-processing of the MRI data. Some of these techniques are rather unrealistic from a fluid mechanics point of view. For example, some authors assume fully developed laminar pipe flow (Efstathopoulos et al. 2008), which is obviously not the case within the aorta.

The present group of authors intend to implement a variational data assimilation (DA) to process the sparse and noisy MRI data and obtain a refined estimate of the flow field. This approach relies neither solely on measurement data nor on numerical simulations, rather these two inputs are used in combination. Data assimilation has already been successfully used on MRI data for two-dimensional flows in Egger et al. (2017). The refined flow field can then be used to improve the estimation of wall shear stress, since the gradient can then be better approximated in the near-wall region. Data assimilation has been used extensively in other fields, for example in meteorology to utilize measurement data from sparse and unevenly distributed weather stations around the globe in numerical computations of weather forecasts (Ghil and Malanotte-Rizzoli 1991). In recent years, DA has experienced increased attention in the fluid mechanics community, especially to refine and improve data from particle image velocimetry (PIV) (Gronskis et al. 2013; Schneiders and Scarano 2016; Yang et al. 2017).

The present approach differs from previous studies, in that a strong emphasis is placed on a preliminary assessment step, in which the reliability of the MRI WSS estimates is first evaluated using comparisons to 'ground truth' or to a 'gold standard'. This notion is not new (Carvalho et al. 2010; Markl et al. 2010, 2011; Potters et al. 2015; Van Ooij et al. 2015), but has often been neglected (D'Elia et al. 2012). The development of such a 'gold standard' is one major goal of the current paper. Lacking such comparisons, some authors resort to comparisons of relative WSS values to each other (Van Ooij et al. 2015), for instance using WSS values before and after a surgical intervention, or WSS values between patients and healthy volunteers measured with the same MRI sequence. Comparability between different studies or research groups is in general relatively poor, since the absolute values remain unknown. Other authors revert to numerical simulations (CFD—computational fluid dynamics), which are often thought to provide a 'gold standard' (Boussel et al. 2009; Piatti et al. 2017). However, this should be viewed critically, since the flow within the aorta can be in the transitional regime between laminar and turbulent, which is extremely challenging even for advanced CFD simulations; hence, the results may be questionable for serving as ground truth (Glaßer et al. 2014). Even if the flow domain is not in the transitional or turbulent regime, results from CFD may vary widely. A good example is the so-called CFD challenges, where different research groups compute the same problem set, i.e., the flow through aneurysms (Berg et al. 2015; Janiga et al. 2015; Steinman et al. 2013; Valen-Sendstad et al. 2018). The disparity between these results is large. Another approach to test WSS estimators is the generation of synthetic flow fields and associated synthetic MRI data, with a subsequent application of the post-processing algorithm (Carvalho et al. 2010; Piatti et al. 2017). However, also this procedure should be viewed critically, since it is unlikely that all influencing physical quantities and noise sources can be properly captured in such synthetic data generation.

In vivo measurements always imply complicated influences such as unknown vessel shape and fluid structure interaction, among others. In this current 'first-step' study, therefore, measurements are performed in vitro with known geometry and flow conditions. The overall accuracy of the WSS estimation can then be compared with known wall shear stress values and any improvements using modified acquisition procedures or processing algorithms can be quantified. The study begins with simple flows and increases complexity step by step, ensuring that the underlying flow conditions are always known. All measurements are performed with both MRV and LDV, the latter serving as a first ground truth. Numerical simulations are conducted in parallel to the experiments and serve as a second ground truth in some cases. To the best of the authors' knowledge, there is no other study attempting to improve WSS estimators obtained from MRV data by comparison to systematic reference measurements.

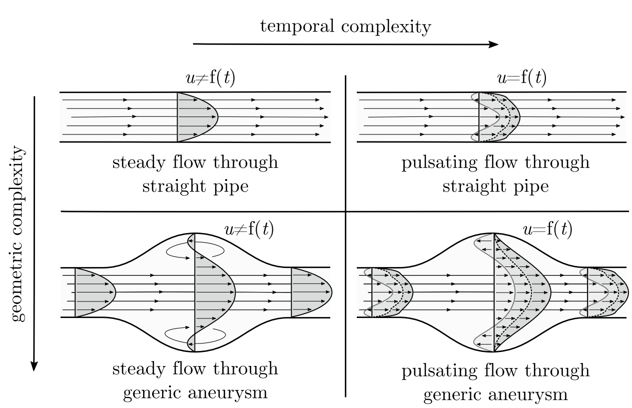

Fig. 1 Stages of abstraction and complexity of the human aorta. This study will focus on the pulsating pipe flow and the steady flow through aneurysms

2 Material and methods

2.1 Abstraction of the human aorta

The human aorta has a complex, patient-specific geometry, which is not very suitable for generic experiments. Also, the flow conditions are far from being analytically accessible or well defined. The objective of the current study is not to investigate flow phenomena within the aorta, but to develop techniques which can serve as ground truth experiments in aorta-like models; hence, some simplifications and abstractions of the aorta are invoked. The stages of abstractions are shown in Fig. 1. The most simple flow is fully developed, laminar, steady pipe flow. The complexity can be increased in the time domain by altering the flow conditions, for instance when a time-varying, cyclic volume flow rate is applied. For a sinusoidal flow rate, this results in sinusoidal pulsating pipe flow, which has been extensively studied in literature. Overviews about pulsating pipe flow can be found in Carpinlioglu and Gündogdu (2001) and Gündogdu and Carpinlioglu (1999a, b). If the pulsation amplitude is large enough, transitional or even turbulent flow can be expected for part of the pulsating cycle. Alternatively, an increase in complexity can be achieved by changing the geometry, for instance using generic aneurysm models. These models can be axially symmetric or asymmetric. The last stage of abstraction is the combination of both geometric and flow complexity, i.e., pulsating flow through generic aneurysms. In the current study, focus will be placed on the pulsating pipe flow as well as on the steady flow through aneurysms.

2.2 Experimental setup

The experimental setup, which is schematically shown in Fig. 2, comprises a portable flow supply unit to generate the desired, time-varying volume flow rates. The flow is then

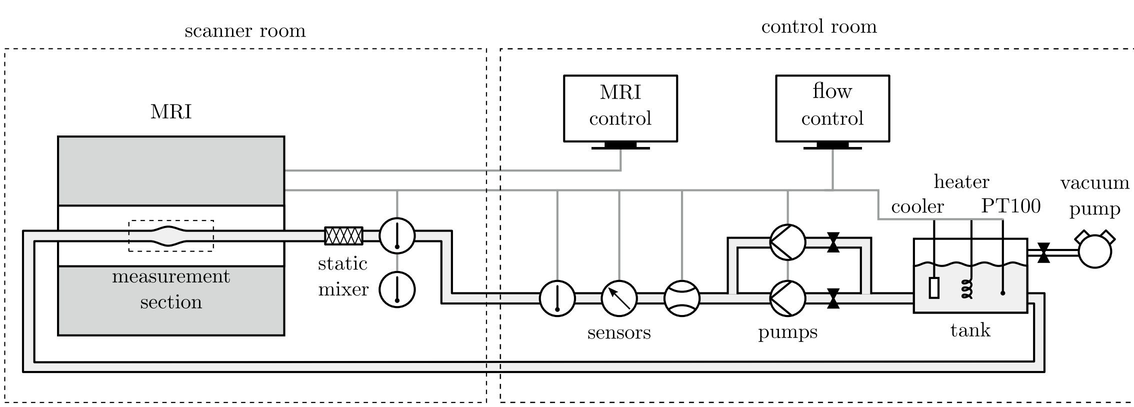

Fig. 2 Experimental setup for the MRV measurements

guided through hoses to the MRV or LDV measurement section.

Water is used as a working fluid. The water is stored in a tank and can be heated with a immersion heater or cooled with a dipping cooler. The temperature in the tank is monitored with thermocouples and the fluid is constantly circulated to ensure a homogeneous temperature distribution. For the MRV experiments, copper sulfate is added as a contrast agent with a concentration of 1 g/L, as suggested by Schenck (1996). For the LDV experiments, the water is seeded with titanium dioxide tracers of approximately 1 µm diameter. The flow supply system contains two different pumps for either steady or unsteady flow conditions. The first pump is a magnetically driven centrifugal pump (RMMSI, Sondermann). The second pump is a gear pump which is driven by a computer-controlled stepper motor (CardioFlow MR 5000, Shelley Med.). Flow waveforms can easily be implemented via built-in software or Matlab^. Downstream of the pumps the flow passes through a high-precision Coriolis flow meter (CORI-FLOW M55, Bronkhorst) with a full-scale range of 10 L/min and an accuracy of 0.2% full scale, which is used for steady flow rates. For unsteady flows, the sensor is not fast enough to follow the measurement value precisely and thus underestimates the amplitudes. The flow rate is therefore extracted from the time-resolved MRV data, as described in Sect. 3.2. The flow supply unit provides a TTL trigger signal for the synchronization of the periodic flow with both the MRI scanner and the laser Doppler signal processor.

The flow is guided from the flow supply unit with hoses of 25.4 mm inner diameter to the measurement section. For the MRV experiments, the pump is placed in the control room next to the MRI scanner room and the hoses are passed through dedicated waveguides of the RF cabin. To ensure fully developed flow conditions at the measurement section, several precautions must be taken. First, all upstream disturbances caused by bends are eliminated with a static mixer (SMX). The design follows the guidelines of Paul et al. (2004) and is based upon the SMX configuration with a total of eight elements, which are shifted at 90° to each other. Afterward, an acrylic tube of d = 26 mm inner diameter and l = 2m length is used as an inlet, corresponding to $l/d \approx 77$. According to Ray et al. (2012), the development length in pulsating pipe flows may be considerably shorter than those for steady flow, which is $l/d \approx 62$ for the current laminar flow conditions. The measurement section consists either of a 0.5 m long straight acrylic tube with 26 mm inner diameter or the aneurysm models with a straight outflow of 0.5 m length.

Special caution is taken regarding secondary flow motion, which is especially evident in the case of laminar flow conditions. When a temperature difference between ambient and fluid is present, density gradients within the water arise and buoyancy forces then introduce an upward or downward motion close to the wall, whereas the inner region experiences a flow in the opposite direction. As a consequence two counter-rotating vortices develop, which shift the velocity maximum toward the top or bottom of the pipe, depending on the sign of the temperature difference. This phenomenon is only apparent in laminar flow, since the mixing process in turbulent flows dominates over buoyancy-induced mixing. A comprehensive description of this effect can be found in Kyomen et al. (1996). Heat exchange is avoided by thermally insulating the pipe and matching the inner and outer temperatures. Both temperatures are therefore measured at the static mixer with two PT100 thermocouples type K. A temperature uniformity in the pipe of ± 0.1 °C is found to be necessary to avoid these secondary flows. Furthermore, the water contains dissolved gases, which originate from the air which is mixed during the flushing process. After a short time small air bubbles coalesce into larger bubbles and disturb the measurement process as well as the flow field. The air is removed with the use of a vacuum pump before each experiment.

2.3 Measurement techniques

The MRV data are acquired with a conventional PC-MRI sequence Markl et al. (2012) without any further acceleration techniques, such as parallel imaging or partial Fourier, in a 3 Tesla whole-body scanner (MAGNETOM Prisma, Siemens Healthcare, Erlangen, Germany). For signal reception, a small flexible coil provided by the system vendor (Flex Loop small) is tightly wrapped around the pipe. Measurement parameters are shown in Table 1. For the pulsating pipe flow, MRI data are acquired for a single transversal slice (slice thickness: 3 mm), with velocity encoding along the through plane direction, i.e., the tube's axial velocity component. For the aneurysm, MRI data are acquired over a three-dimensional, axially oriented volume with velocity encoding in all three spatial directions. The two-dimensional PC-MRI measurements are repeated three times and subsequently averaged to increase SNR. Because of limited measurement time, signal averaging was not done for the aneurysms. The velocity encoding value *venc* is chosen lower than the maximum velocity, thus phase wraps of the first and second order are apparent, which, however, improves the velocity–noise ratio in regions with smaller velocity values. Phase wraps are semi-automatically corrected with an algorithm described in Bruschewski et al. (2014). Every measurement includes a so-called flow-off measurement for which the pump is switched off. The flow-off data are used to retrospectively correct systematic background phase errors induced, e.g., by Eddy currents.

The laser Doppler data are obtained using a two-velocity component laser Doppler system (Flow Explorer, Dantec

Table 1 MRV measurement parameters

No.	Type	Voxel size (mm)	*venc* (m/s)	TE (ms)	TR (ms)	Phases (–)	Repetitions (–)
1	2D1C + time	$0.5 \times 0.5 \times 3$	0.05	8.0	45.2	59	3
2	2D1C + time	$0.4 \times 0.4 \times 3$	0.10	6.1	37.6	71	3
3	2D1C + time	$0.4 \times 0.4 \times 3$	0.20	5.2	34.0	79	3
4	3D3C	0.5 isotropic	0.02	11.6	58.4	–	1
5	3D3C	0.5 isotropic	0.25	6.9	39.2	–	1

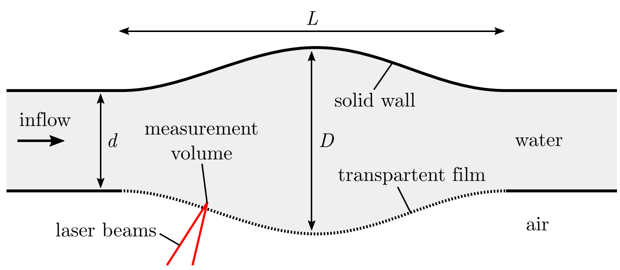

Fig. 3 Schematic view of the aneurysm model. The transparent film allows optical accessability without disturbing the flow

Dynamics). The wavelength of the laser is $\lambda = 660$ nm and a short focal length of $f = 150$ mm is used to reduce the size of the measurement volume and obtain measurements as close to the wall as possible. The size of the measurement volume is estimated to be 331 μm × 49 μm × 49 μm with the first dimension designating the radial (wall-normal) direction. All measurements are carried out on the center axis of the pipe, where refraction due to different refractive indices is only present along one direction. The LDV head is mounted onto a traverse (MS200HT, ISEL) with $\Delta x = 0.0125$ mm minimum step size.

2.4 Aneurysm models

The geometry of the aneurysm, shown in Fig. 3, is axially symmetric with a smooth expansion of the diameter. The shape is based upon the work of Budwig et al. (1993), Peattie et al. (2004) and Salsac et al. (2006) with an inlet diameter equal to those of the straight pipe of $d = 26$ mm and a length of $L = 104$ mm, corresponding to $L/d = 4$. The maximum diameter of the phantom is $D = 65$ mm, thus $D/d = 2.5$.

The model is fabricated from polyamide using a laser powder bed fusion process. Optical access for the LDV measurements is ensured through a slit in the model in the axial direction. The slit is covered with a 0.5 mm thick transparent film of polycarbonate, which is glued to the inner surface of the model. Before insertion of the transparent film, the film is thermoformed onto a negative form of the aneurysm, ensuring a smooth transition without any sharp edges.

Due to the curved surface, measurements are restricted to 0.5 mm away from the wall. This technique for obtaining optical access was tested prior to the measurements using a straight pipe of known flow conditions, where no influence of the transparent film was observed.

2.5 Flow conditions

Three cases of pulsating pipe flow are examined, covering all relevant flow regimes. Sinusoidal pulsating pipe flow in general is the composition of a constant flow and a sinusoidal oscillating flow in the form of:

$$Re(t) = Re_{\text{mean}} + Re_{\text{amp}} \sin(\omega t), \tag{1}$$

where the constant flow is expressed via the time mean Reynolds number $Re_{\text{mean}} = U_{\text{mean}} d/\nu$, based on the pipe diameter d, with ν being the kinematic viscosity. The time-dependent oscillation is expressed with the amplitude of the oscillating Reynolds number $Re_{\text{amp}} = U_{\text{amp}} d/\nu$ and a frequency ω, which is expressed dimensionless as the Womersley number $Wo = \sqrt{\omega/\nu}\, d/2$.

The first case to be examined is a laminar sinusoidal pulsating pipe flow, with a mean Reynolds number of $Re_{\text{mean}} = 1038$ and an amplitude of $Re_{\text{amp}} = 596$. The second and third flows examined represent realistic flow conditions for the human aorta. Their time-dependent flow rate is very similar to those from Salsac et al. (2006) and shown in Fig. 4. The first physiological pulsating pipe flow has a maximum of $Re_{\text{max}} = 3952$, and the second flow $Re_{\text{max}} = 7651$, corresponding to the resting and exercise conditions of a patient.

For the flow through the aneurysms, steady flow rates of $Re_{\text{mean}} = 1998$ and $Re_{\text{mean}} = 5320$ are investigated. For the turbulent flow, the shear Reynolds number $Re_\tau = u_\tau R/\nu$, based on the friction velocity u_τ and the pipe radius R, is $Re_\tau = 180$.

Time-dependent experiments are conducted at a Womersley number of $Wo \approx 20$, characteristic for the ascending and descending aorta (Caro 2012). All flow conditions are summarized in Table 2.

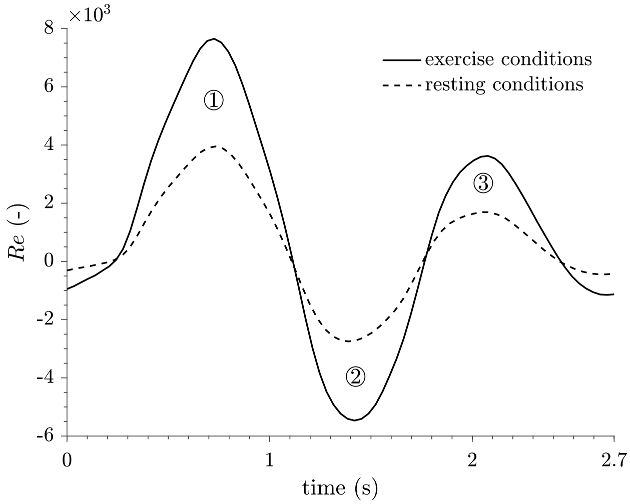

Fig. 4 Reynolds numbers corresponding to resting and exercise conditions in the human aorta. Numbers refer to the points where the velocity profiles are analyzed. Adapted from Salsac et al. (2006)

2.6 Reference data

2.6.1 Analytic data

For the laminar pulsating pipe flow, there exists an analytic solution, first developed by Womersley (1955). The following mathematical description is based upon the work of Brenn (2016), Durst et al. (1996a) and Lambossy (1952).

For an incompressible fluid of constant density ρ and dynamics viscosity μ, the Navier–Stokes equation simplifies for the case of only one velocity component, here in axial direction, to:

$$\rho \frac{\partial u}{\partial t} = \frac{\partial p}{\partial x} + \mu \left(\frac{\partial^2 u}{\partial r^2} + \frac{1}{r} \frac{\partial u}{\partial r} \right). \tag{2}$$

Due to the linearity of this simplified Navier–Stokes equation, the pressure term can be decomposed into its n harmonic parts:

$$\frac{\partial p}{\partial x}(t) = P_0 + \sum_{n=1}^{N} P_n e^{i\omega_n t}, \tag{3}$$

with the harmonic frequencies ω_n and the unknown pressure coefficients P_0 and P_n. These coefficients can be determined with the use of the time-varying volume flow rate $V(t)$:

$$V(t) = V_0 + \sum_{n=1}^{N} V_n e^{i\omega_n t} = \iint u(r,t)\,\mathrm{d}A, \tag{4}$$

which can be measured. This set of equations can be solved to obtain the velocity field in the straight pipe:

$$u(r,t) = \frac{2V_0}{\pi R^2}\left(1 - \frac{r^2}{R^2}\right) + \Re\left\{ \sum_{n=1}^{N} \frac{V_n}{\pi R^2} \frac{1 - \frac{J_0\left(\Lambda_n \frac{r}{R}\right)}{J_0(\Lambda_n)}}{1 - \frac{2}{\Lambda_n}\frac{J_1(\Lambda_n)}{J_0(\Lambda_n)}} e^{i\omega_n t} \right\}, \tag{5}$$

with $\Lambda_n = Wo_n i^{3/2}$, the Womersley number $Wo_n = R\sqrt{\omega_n/\nu}$, pipe radius R, the measured coefficients of the varying volume flow rate V_0 and V_n, and the Bessel functions of the first kind, nth order J_n. The wall shear stress is calculated from the gradient at the wall, $r = R$:

$$\tau_\mathrm{w} = \frac{4V_0\eta}{\pi R^3} + \Re\left\{ \sum_{n=1}^{N} \frac{V_n \eta}{\pi R^3} \frac{\frac{\Lambda_n J_1(\Lambda_n)}{J_0(\Lambda_n)}}{1 - \frac{2J_1(\Lambda_n)}{\Lambda_n J_0(\Lambda_n)}} e^{i\omega_n t} \right\}. \tag{6}$$

2.6.2 Numerical simulations

For the laminar flow through the aneurysm, there exists no analytic solution; therefore, numerical computations at the Reynolds number $Re = 1998$ provide comparison data of the velocity field and associated wall shear stress. The total length of the solution domain (Fig. 5) covering the aneurysm geometry is $13d$, with the inflow and outflow pipes being $4d$ and $5d$ long, respectively. The computational mesh comprises 1,180,608 cells; the cross-sectional area is meshed by 5625 cells; see Fig. 6 for the grid

Table 2 Flow conditions for the conducted experiments

No.	Geometry	Flow	Re (−)	T (s)	Wo (−)
1	Pipe	Sinusoidal pulsating	$Re_{mean} = 1038$, $Re_{amp} = 596$	2.7	20.1
2	Pipe	Physiological pulsating	Resting conditions, $Re_{max} = 3952$	2.7	20.3
3	Pipe	Physiological pulsating	Exercise conditions, $Re_{max} = 7651$	2.7	20.3
4	Aneurysm	Steady	$Re_{mean} = 1998$	–	–
5	Aneurysm	Steady	$Re_{mean} = 5320$	–	11

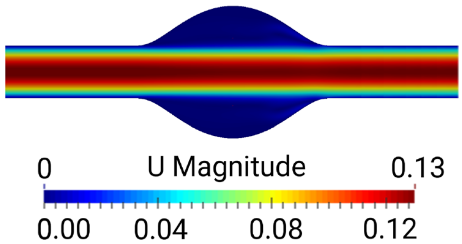

Fig. 5 Flow domain of the aneurysm configuration investigated computationally at $Re = 1998$, illustrating the mean axial velocity field

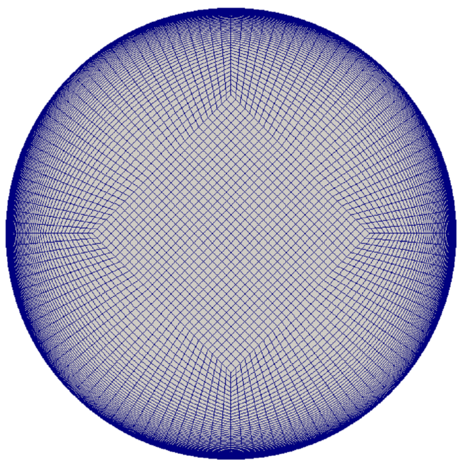

Fig. 6 Details of the numerical grid arrangement in the cross section of the aneurysm geometry

arrangement in the cross section of the aneurysm geometry revealing hexahedral mesh structure. The grid resolution is appropriately fine; e.g., the maximum dimensionless height (normalized by corresponding viscous length ν/U_τ) of the wall-next cells within the entire flow domain is $\Delta y^+ \leq 0.05$. The face lengths of the coarsest cell situated at the symmetry axis within the aneurysm section correspond to $(\Delta x^+, \Delta y^+) = (1.4, 1.4)$, Fig. 6; the corresponding cell face length in the axial direction is $\Delta z^+ = 2.0$. Further grid refinement (the results are not shown here) did not result in any noticeable difference. Inflow was generated by a precursor simulation of the fully developed flow in a $2d$ long pipe. The zero-gradient boundary condition is applied at the outflow cross section. The discretization of both convective and diffusive transport terms is achieved using the second-order accurate central differencing scheme. The fully developed inflow conditions are in agreement with the experimental investigations, performed with a $96d$ long inflow pipe. The computations have been performed with the finite volume-based open source toolbox OpenFOAM®, employing the SIMPLE procedure for coupling the velocity and pressure fields.

3 Pulsating pipe flow

3.1 Post-processing of the LDV data

For the calculation of the wall shear stress from laser Doppler data, the exact position of the wall needs to be determined. Prior to each LDV measurement in the straight pipe, a reference measurement is conducted in a steady turbulent pipe flow of $Re \approx 5300$ to determine the position of the wall. The validation settings of the laser Doppler signal processor are adjusted so that no signal is detected when the measurement volume is fully embedded in the wall. When the measurement volume lies partially within the wall and partially in the flow, the flow velocity is overpredicted (Durst et al. 2004), as shown in Fig. 7. The position of the wall is determined from the measured velocity profile using a linear fit through the nearest measurement points which do not lie within the wall. The data rate increases to the point where the measurement volume is completely within the fluid and decreases with increasing distance to the wall due to diffuse light scattering of the highly seeded flow (Fig. 7). The calculated position of the nearest available measurement point to the wall is in accordance with the theoretically predicted length of the semi-axis of the measurement volume. All subsequent LDV measurements are corrected for position with this reference.

3.2 Post-processing of the MRV data

Since all experiments are conducted within axisymmetric pipes, a mean velocity profile can be obtained by azimuthal averaging. First, the magnitude data are used to segment

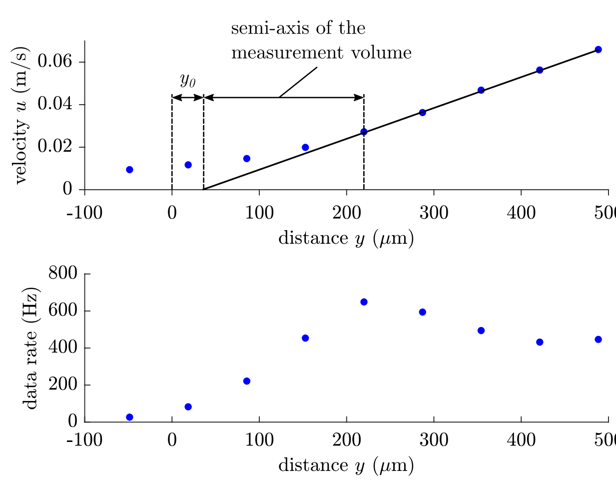

Fig. 7 Top: correction of the position for laser Doppler measurements in the vicinity of the wall. y_0 corresponds to the initial guess. Bottom: data rate increases as the measurement volume is moved into the flow domain

the signals of the flow model from surrounding noise. If the magnitude data are less than a certain threshold, the corresponding voxel in the phase image is masked out. The threshold is calculated based on a method proposed by Otsu (1979), using the histogram of the magnitude. After segmentation, the volume flow rate is extracted as the sum of the remaining voxels. The midpoint of the circular-shaped pipe is detected within Matlab® using the approach of Atherton and Kerbyson (1999). Starting from this point, the radius of each voxel can be determined. The voxels are grouped into bins of $\Delta y = 0.2$ mm along the radius. For the calculation of the wall shear stress, the position of the wall, where the no-slip condition is assumed, is determined from the pipe diameter. The WSS is calculated with a linear gradient between the wall and the second measurement point inside the flow field, because the first measurement point was subject to systematic errors caused by partial volume effects. To avoid conflicts with potential asymmetric flow conditions, the flow field is divided into 12 equally spaced segments around the circumference; see Fig. 8. This method is common for in vivo measurements, where the flow is typically not symmetric (Frydrychowicz et al. 2009; Harloff et al. 2013, 2010). For each segment, the velocity and WSS are calculated separately.

The velocity uncertainty of the MRV data is estimated from the background noise of the magnitude data. Where possible, the uncertainty is measured directly within the region of interest by subtracting two consecutive measurements, which may give better results (Bruschewski et al. 2016). For the pulsating pipe flow, the relative uncertainty with respect to the maximum velocity is determined to be approximately 2.4%, and 5% for the aneurysms. However, due to the circumferential averaging, the uncertainty reduces significantly.

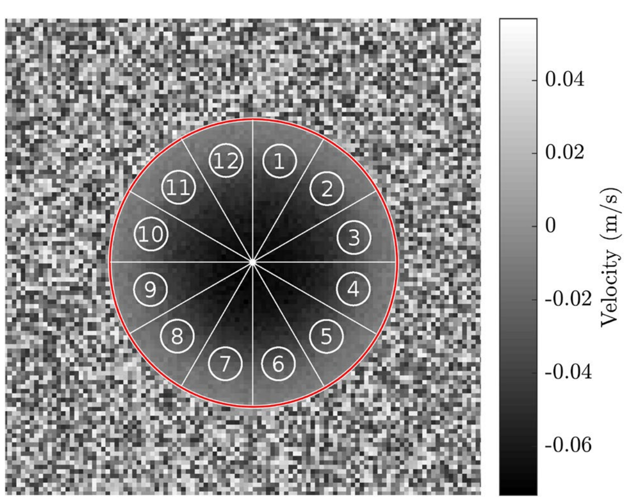

Fig. 8 Velocity field in the straight pipe. The detected geometry (red) is divided into 12 equally spaced segments

3.3 Laminar sinusoidal pulsating pipe flow

The velocity profile of the laminar sinusoidal pulsating pipe flow, shown in Fig. 9, is evaluated at three characteristic time steps, which correspond to the instants of maximum, minimum and zero crossing of the volume flow rate. The analytic solution exhibits the characteristic parabolic velocity profile for laminar flows in the middle of the pipe. Near the wall, the profile deviates from its steady solution due to the periodic change of the volume flow rate. Although the net volume flow rate is always positive, the flow experiences considerable back flow in the region near the wall, where viscous effects dominate over inertia forces. The red area represents the region, in which the velocity profiles of the 12 segments fall. Thus, this value gives an indication of the symmetry of the flow. The red dots represent the mean value over all segments. The velocity profile shows small deviation from its symmetric values, especially for the time at maximum Reynolds number. However, the deviations become much smaller at the region near the wall. The laser Doppler and mean MRV data are in excellent agreement with the analytic prediction for all time steps.

The wall shear stress from the LDV is calculated from a refined velocity measurement near the wall (not shown here). The gradient is calculated between the wall, where the no slip condition is assumed, and the first point totally inside the flow. This point is chosen according to the procedure described above for determining the wall position and is usually in the range 160 µm < y < 200 µm. In Fig. 10, and the resulting wall shear stress τ_w is shown over the angle ϕ of the cycle. The laser Doppler data can capture the value of the wall shear stress very well. In the lower region, the LDV data experience a slight underprediction of the amplitude

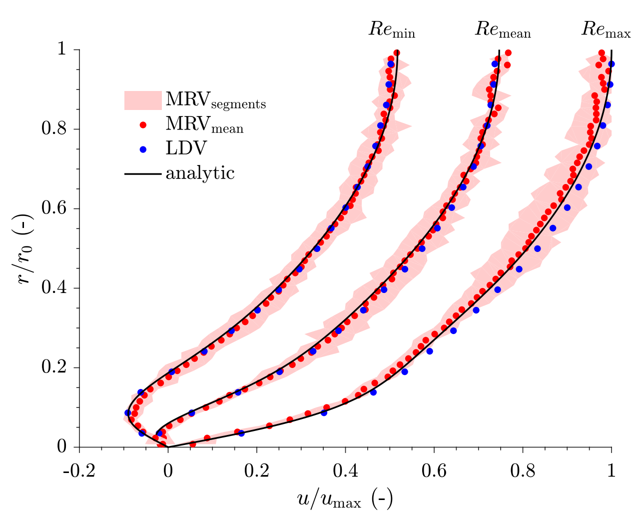

Fig. 9 Velocity profile of the laminar sinusoidal pulsating pipe flow. Note that the resolution of the MRV data appears finer due to the circumferential averaging

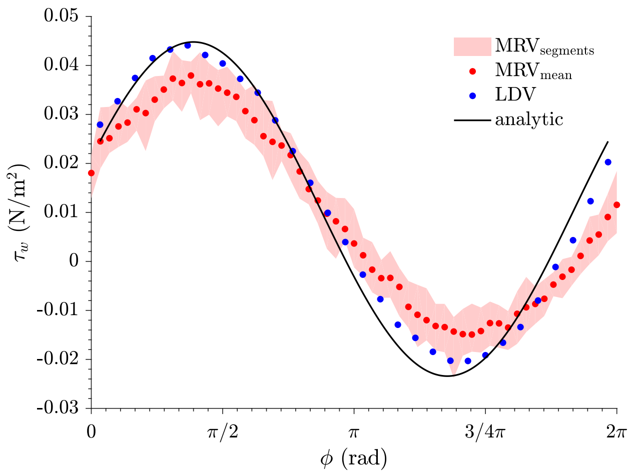

Fig. 10 Estimation of the wall shear stress for the laminar sinusoidal pulsating pipe flow, in comparison to the analytic solution

of the wall shear stress as well as some minor phase shift. The MRV data show a significant underprediction of the amplitude of about 25%. Again, a phase shift is noticeable. The red area marks the variations of the WSS between the individual pipe segments.

3.4 Physiological pulsating pipe flow at resting conditions

The velocity profile of the physiological pulsating pipe flow at resting conditions is shown in Fig. 11. The velocity shown is evaluated at the three peaks of the volume flow rate, which are maximum, minimum, and the second maximum, as indicated in Fig. 4. The laminar solution is calculated from Eq. 5 with the cyclic volume flow rate. Due to the higher frequencies present in the flow, compared to the sinusoidal case, the velocity profile has a very flat shape in the pipe center. Although the maximum Reynolds number is $Re_{\max} = 3952$, the velocity profile from both MRV and LDV measurements match perfectly the laminar solution. The accelerating motion appears to have a stabilizing effect on the flow, which is in accordance with previous findings (Iguchi and Ohmi 1984). The flow is quasi-symmetric in circumferential direction. Deviations between the individual pipe segments are insignificant.

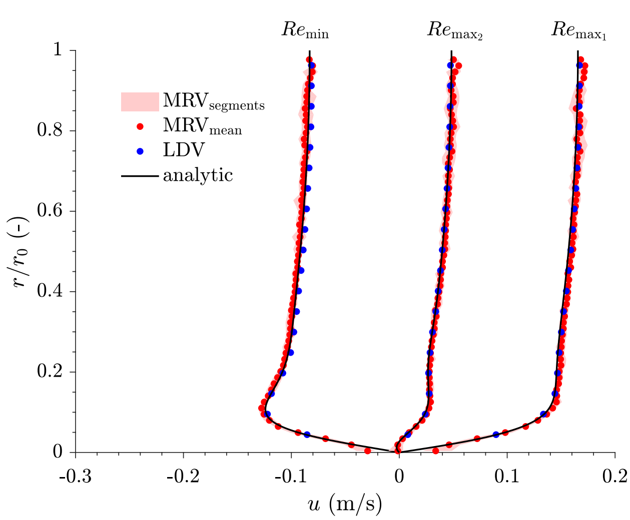

Fig. 11 Velocity profile of the physiological pulsating pipe flow at resting conditions. Note that the resolution of the MRV data appears finer due to the circumferential averaging

The temporal evolution of the wall shear stress is depicted in Fig. 12. Although the flow waveform appears to have a smooth evolution in time, the wall shear stress experiences some additional curvature. The large peak at the beginning of the cycle has roughly the same value of the wall shear stress as the second, minor peak, while the largest amplitude originates from the backflow. The laser Doppler is able to follow even the smaller excursions in the WSS. The data show a slight underprediction of the amplitude of the theoretical value with a small phase shift. The WSS from the MRV measurements shows a larger underprediction and in accordance with this a larger phase shift. The deviation of the WSS over the individual segments is minor.

3.5 Physiological pulsating pipe flow at exercise conditions

The velocity profile of the physiological pulsating pipe flow, shown in Fig. 13, is almost equal in shape to the velocity profile from resting conditions. The curvature in the vicinity of the wall is slightly higher. One would expect the flow to be turbulent, with the maximum Reynolds number being $Re_{\max} = 7651$. As can be seen from the

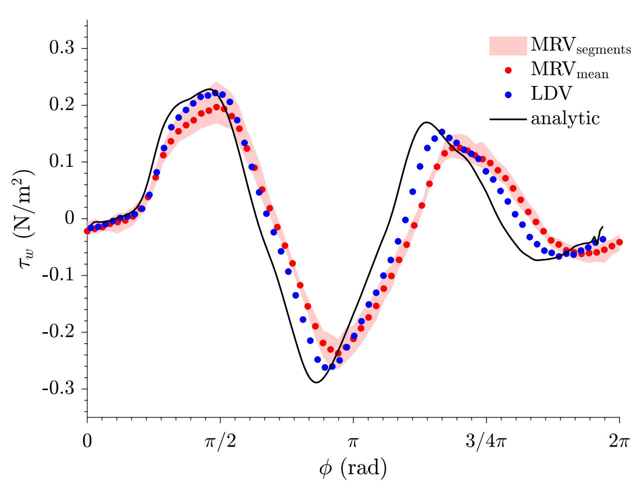

Fig. 12 Wall shear stress of the physiological pulsating pipe flow at resting conditions, in comparison to the analytic solution

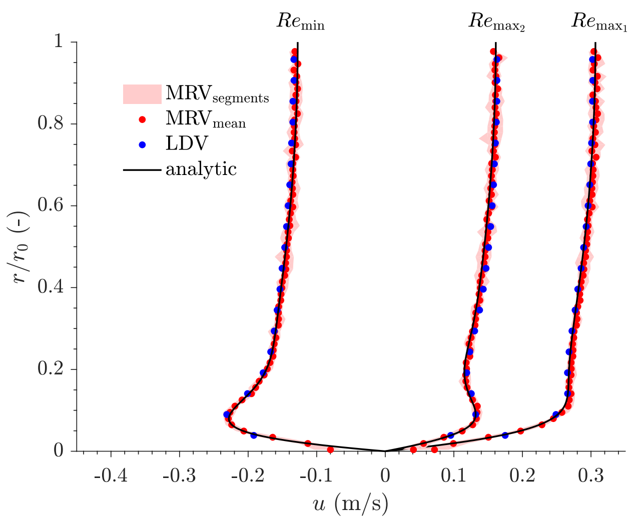

Fig. 13 Velocity profile of the physiological pulsating pipe flow at exercise conditions. Note that the resolution of the MRV data appears finer due to the circumferential averaging

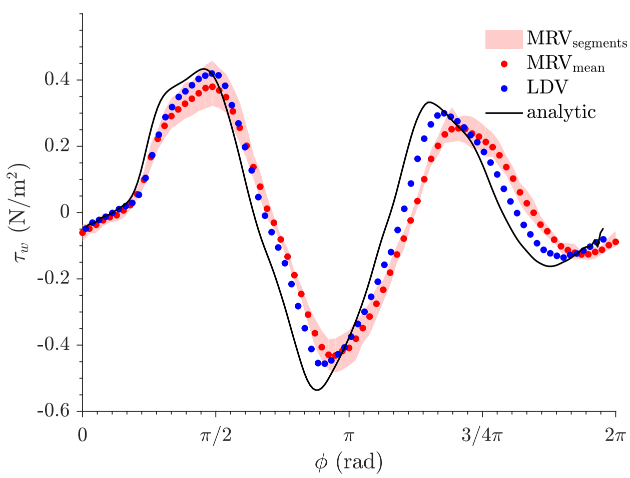

Fig. 14 Wall shear stress of the physiological pulsating pipe flow at exercise conditions, in comparison to the analytic solution

velocity profile in comparison to the analytic reference data, this is not the case. Again all measurement data are in perfect agreement with the laminar solution. In addition, the flow is again perfectly symmetric

The shape of the temporal wall shear stress is similar to that in the resting conditions (Fig. 14). The laser Doppler shows a slightly larger underestimation of the amplitude than in the former case and has a more significant phase shift. The MRV data again underestimates the WSS in the same order as that for the resting conditions. In general, the differences between resting and exercise conditions regarding underpredictions of the expected values is minor.

4 Steady flow through aneurysm

4.1 Flow phenomena

Figure 15a shows the velocity field in the middle of the aneurysm, obtained from the MRV measurement at a mean Reynolds number of $Re = 1998$. The steady flow enters the aneurysm from the left and detaches from the wall due to the steep expansion and the associated adverse pressure gradient at about $x/d \approx -2$, where x is the coordinate in axial direction, measured from the location of maximum diameter. Resulting from the detachment of the flow, a large recirculation zone forms in the middle of the aneurysm. The flow reattaches at an axial distance of $x/d \approx 2$. In the vicinity of the resulting stagnation point, shown in Fig. 15b, large velocity gradients exist in the radial and axial direction, suggesting high local wall shear stress with large spatial variations.

Results from Budwig et al. (1993), which are shown in Fig. 15c, confirm that the wall shear stress experiences high spatial variations around the detachment point and in the local vicinity of the reattachment point. Downstream of the detachment point, the wall shear stress reaches a minimum value, slightly below zero, due to the small negative velocities in the recirculation zone. At the reattachment point, the wall shear stress shows a continuous decrease followed by a sudden increase, reaching a global maximum of about $\tau_w/\tau_{w_0} = 2.2$. In the turbulent flow with $Re = 5320$, the same characteristics are observed.

For clinical studies, these spatial variations may be the key factor for the development and growth of enlargements, as suggested by Boussel et al. (2008) and Meng et al. (2007). The challenge for in vivo measurements and post-processing algorithms is to properly resolve this variation.

For these reasons, the focus for the LDV reference measurements is placed on a small region around the peak of the wall shear stress, downstream of the reattachment point, marked in Fig. 15c.

4.2 Post-processing of the MRV data

For the calculation of the wall shear stress from MRV data, the same azimuthal averaging process is applied as for the pulsating pipe flow. The boundary of the geometry is determined as follows. First, the midpoint and radius within each slice in axial direction are determined by finding the boundary with the method described in Atherton and Kerbyson (1999). This also provides information about the local aneurysm diameter. Using the resulting center axis and the location of maximum diameter, the

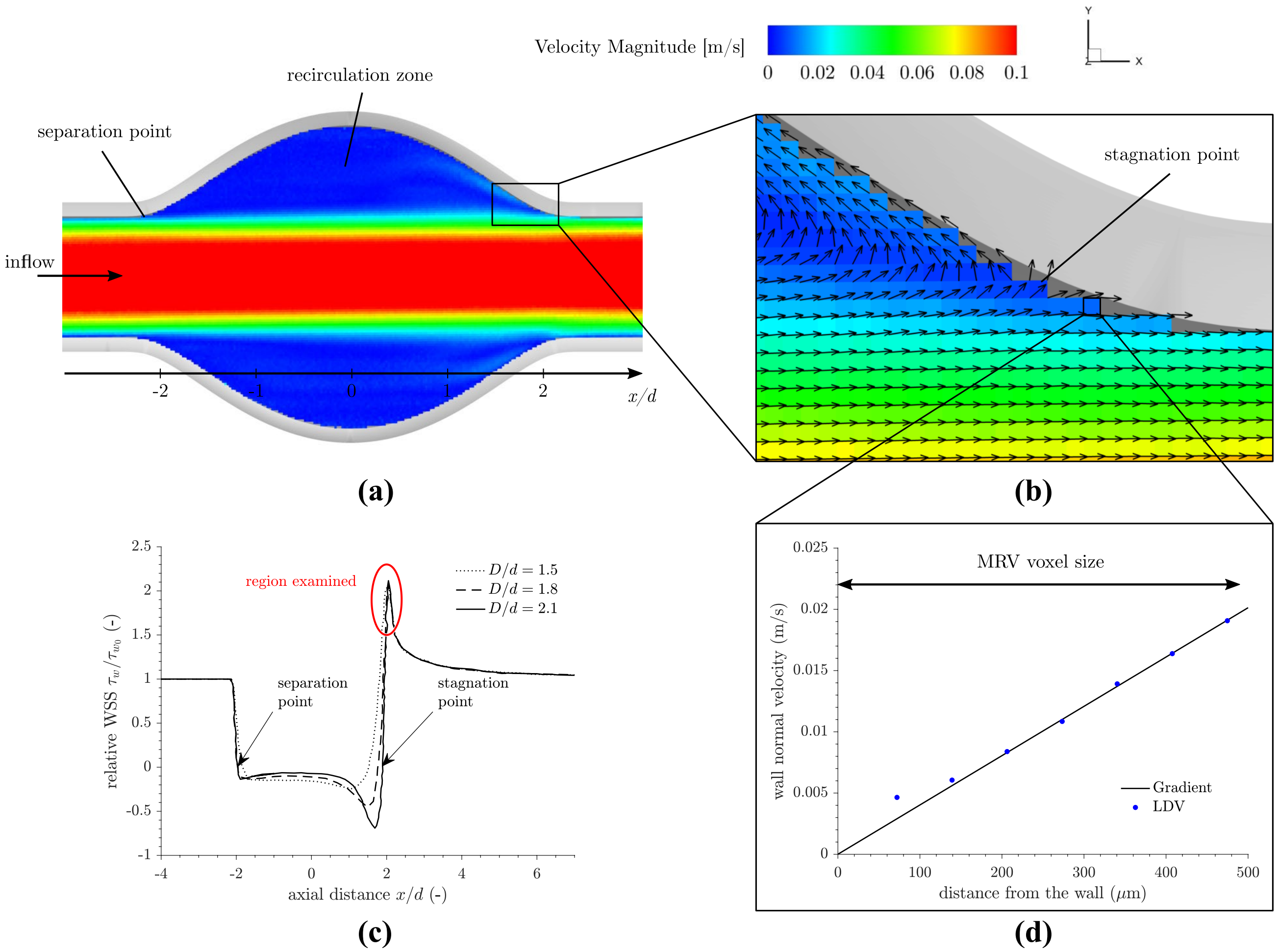

Fig. 15 **a** Velocity magnitude of the MRV data in the middle of the aneurysm geometry at $Re = 1998$. **b** Close-up view of the MRV data in the region near the point of reattachment, where local variations in the velocity lead to high spatial gradients of the wall shear stress. **c** Results from Budwig et al. (1993) in different geometries for laminar flow show high spatial variations of the WSS. The region examined in this work is highlighted. **c** Exemplary LDV measurement at an axial distance of $x/d = 2.1$. **d** Exemplary LDV measurement at an axial distance of $x/d = 2.1$

known geometry of the aneurysm is positioned. The wall shear stress is subsequently calculated in the wall-normal direction from the boundary with the tangential velocity, using the built-in function of Matlab® *improfile*.

4.3 Laminar flow

For the laminar flow conditions, the region at the wall, where a nearly linear velocity profile prevails, is large enough to apply the same procedure as described in Sect. 3.1, shown in Fig. 15d. Neighboring measurement points are located at a distance of $\Delta y = 50$ μm. A linear fit is used to determine the gradient, while the measurement points which lie partially within the wall are omitted.

The results for the laminar flow through the aneurysm are shown in Fig. 16. The laser Doppler is able to capture the position of the peak wall shear stress as well as its magnitude. The numerical simulation is in excellent agreement with the experimental results. The computation is challenging, since even small upstream variations in the flow may influence the separation and reattachment points, and thus the local wall shear stress. In comparison to the results from Budwig et al. (1993), the peak is shifted approximately $x/d \approx 0.3$ upstream. The deviations from the wall shear stress in axial direction in comparison to results from Budwig et al. (1993) may be caused by a slightly different shape of the aneurysm, which was not completely documented in Budwig et al. (1993).

The wall shear stress from the MRV data exhibits a systematic underestimation, especially in the regions of higher wall shear stress amplitudes. The shaded area indicates that the laminar flow is not perfectly symmetric, but this asymmetry does not increase over the aneurysm length.

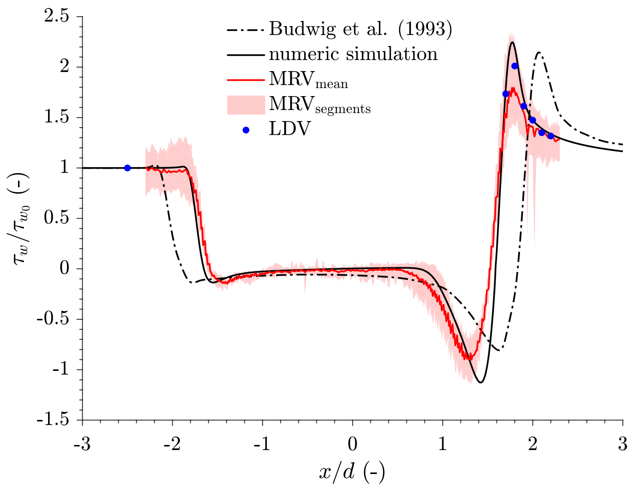

Fig. 16 Experimental data compared to computational results for the wall shear stress distribution along the axial distance in the aneurysm for $Re = 1998$. τ_w is normalized with respect to the measured value in the straight pipe upstream of the expansion

4.4 Turbulent flow

Although the measurement grid for the laser Doppler is refined to $\Delta y = 25$ µm in the turbulent flow through the aneurysm, the determination of the gradient remains challenging. Only a few points remain in the linear region of the boundary layer velocity profile, contrary to the turbulent pipe flow used in Sect. 3.1. In the following section, four different approaches for the estimation of τ_w from the LDV data are discussed.

The first method is a manual estimation of the gradient by visual inspection of the velocity profile. Usually, this method results in the choice of the steepest gradient.

As suggested by many other authors (Clauser 1956; Kendall and Koochesfahani 2008; Rodríguez-López et al. 2015), the data points which lie outside the linear region may contribute as well to the calculation of the wall shear stress.

For turbulent flows there exist a more or less universal shape of the velocity profile when nondimensionalized. In a small region in the vicinity of the wall, where viscous forces are dominant, the velocity profile follows a linear relationship $u^+ = y^+$, where u^+ and y^+ are denoted as the dimensionless wall coordinates. These are given by the definitions $u^+ = \bar{u}/u_\tau$ and $y^+ = yu_\tau/\nu$ with the wall shear velocity defined as $u_\tau = \sqrt{\tau_w/\rho}$. This relation is valid for $y^+ < 5$. For $y^+ > 30$, a logarithmic law in the form of $u^+ = 1/\kappa \ln(y^+) + B$ applies, while the constants κ and B may slightly vary for different types of flows (Rodríguez-López et al. 2015). In the intermediate region ($5 < y^+ < 30$), a buffer layer is present, smoothly connecting both regions.

The second and third methods to estimate τ_w are based upon this universal shape of the velocity profile. The principle used is described in Kendall and Koochesfahani (2008), while a good overview about other techniques can be found in Rodríguez-López et al. (2015). The wall shear stress and the position of the wall are iteratively determined by fitting the measurement data to the aforementioned law of the wall or other empirically or numerically derived velocity profiles. The measured mean velocity $\bar{u}$ is normalized with respect to the friction velocity u_τ to obtain u^+ and the wall-normal coordinate is expressed in the form of:

$$y^+ = (y + y_0)\frac{u_\tau}{\nu}, \tag{7}$$

where y_0 is a possible offset of the wall distance. The values of u_τ and y_0 are chosen iteratively to fit the measurement data to the model. The optimal values for u_τ and y_0 are determined with the minimum of the residual function:

$$\Phi = \frac{1}{N}\sum_{i=0}^{N}\frac{|u_i^+ - u_{i,\text{model}}^+|}{u_i^+}, \tag{8}$$

which is a measure of the difference between the measured data points u_i^+ and the model data points $u_{i,\text{model}}^+$. The residual function gives more weight to data points near the wall. The wall shear stress is calculated from $\tau_w = u_\tau^2\rho$. For the first model, the data are fitted to the velocity profile developed by Musker (1979). It is valid from the viscous sublayer to the logarithmic region and is given in the implicit form of:

$$\frac{du^+}{dy^+} = \frac{\frac{(y^+)^2}{\kappa} + \frac{1}{s}}{(y^+)^3 + \frac{(y^+)^2}{\kappa} + \frac{1}{s}}, \tag{9}$$

with $\kappa = 0.41$ and $s = 0.001093$.

The second velocity profile used as a model are the data from a direct numerical simulation (DNS) of a turbulent pipe flow at $Re = 5300$ from El Khoury et al. (2013). The axisymmetric geometry of the aneurysm motivated the use of this data set. Results are shown in Fig. 17.

The last method to calculate τ_w is the one proposed by Durst et al. (1996b), which fits the measurement data to a model of the form:

$$u = \frac{u_\tau^2}{\nu}(y - y_0) + C_2(y - y_0)^2 + C_4(y - y_0)^4 + C_5(y - y_0)^5, \tag{10}$$

with the free fitting parameters C_2, C_4, C_5, u_τ and y_0. This method satisfies the momentum equation, but is restricted to the region $y^+ < 12$.

The results of all four methods are shown in Fig. 18. The LDV measurements are in very good agreement with each other. All LDV post-processing methods show a peak of τ_w at $x/d = 1.8$. In general, the methods from Musker (1979)

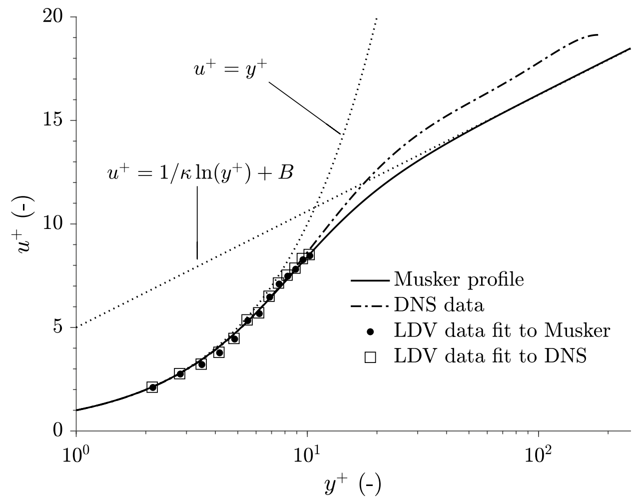

Fig. 17 Velocity profiles in wall coordinates, including an exemplary fit of the measured LDV data at $x/d = 1.75$

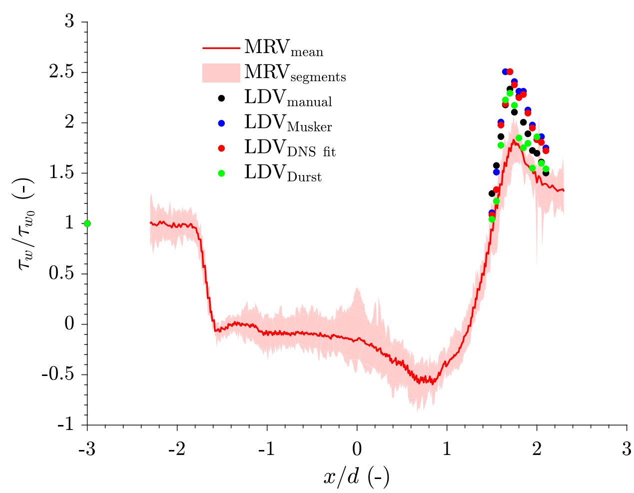

Fig. 18 Wall shear stress distribution for different LDV post-processing methods, compared to MRV data in the aneurysm for $Re = 5320$

and DNS data differ only slightly. In comparison, the manual assessment yields lower values, owing to the steep gradient and the few points inside the linear region. The method proposed by Durst et al. (1996b) gives comparable results, but the data exhibit higher scatter. In this turbulent regime, the reason for the very similar results from the fits to the velocity profile from Musker (1979) and the DNS is the very similar velocity profile near the wall and the fact that the LDV data were restricted to this area (Fig. 17). The reason for the highly scattered results obtained with the method proposed by Durst et al. (1996b) is unknown, but the method may be more sensitive to measurement errors.

The MRV data underestimates the local wall shear stress especially in the region of the peak. The magnitude of this deviation is comparable to deviations obtained from the laminar flow through the aneurysm and the pulsating pipe flow from Sect. 3. In contrast to the laminar flow, the symmetry before and after the aneurysm is less significant, but there exists a larger scatter in the recirculation zone. It has to be mentioned, that the turbulent flow field shows a high degree of non-uniformity due to turbulent velocity fluctuations. The shaded area in this case is not only a measure for asymmetry, but also represents turbulent fluctuations.

In summary the LDV is able to capture the wall shear stress of the complex geometry of a model aneurysm and is able to identify regions where τ_w may affect the local behavior of the vessel walls.

5 Discussion and conclusions

One of the main purposes of the present study was to fabricate a flow facility in which various flow conditions—steady, pulsating/oscillating—for various flow geometries—pipe flow, aneurysm models—could be generated with a high degree of reproducibility while being suitable for both MRV and LDV measurement of the wall shear stress. This goal has been achieved. The test facility exhibited a high degree of reproducibility, demonstrated in particular for the pulsating pipe flow. Excellent agreement of the flow conditions was achieved for LDV and MRV experiments, despite the fact that the measurements were conducted consecutively on different days. This is considered a pre-requisite for the subsequent critical assessment of the wall shear stress measurements obtained using MRV through comparison with nominally more accurate methods, either LDV, analytic solutions or numerical simulations.

While analytic solutions are preferable as a ’gold standard’, they do not exist for the complex flow conditions eventually to be encountered with in vivo measurements; hence, a second goal of this study was to demonstrate that wall shear stress measurements using LDV could be used as a substitute standard, where feasible. Despite the complex geometry of an aneurysm, the present results indicate that WSS measurements using LDV are indeed feasible; however, careful consideration must be taken in evaluating the influence of the finite detection volume size. In general, the limiting factor for reasonable estimations of the WSS using LDV is the spatial resolution. The deviation from the expected values, especially in Figs. 12 and 14, originates most likely from the finite size of the measurement volume. With the current LDV setup, the minimum distance from the wall where accurate measurements can be performed is about the semi-axis of the measurement volume size, thus 165 µm. Theoretical considerations from the laminar analytic velocity profile show that the wall shear stress from a linear gradient between the nearest possible LDV point to the wall coincide well with the measured values. A detailed description can be found in Bauer et al. (2018). Even though the velocities in the investigated models, especially in the vicinity of the wall, were close to zero, and high spatial resolution was required, the LDV results for τ_w were excellent. For unsteady flow conditions, the time varying wall shear stress could be resolved in the flow of a pulsating pipe flow and excellent agreement with the analytic solution could be achieved. The finite size of the measurement volume led to minor underestimations of the wall shear stress. However, the measurement in a complex geometry of an aortic aneurysm showed good agreement with the numerical predictions as well as with values from literature.

Although the velocity profiles obtained from MRV and LDV for the sinusoidal pulsating pipe flow show excellent agreement, the WSS from the MRV data is found to depend highly on the averaging process as well as on the exact choice of points taken into the calculation of τ_w.

Nevertheless, the current work demonstrates that WSS estimation from MRV data is feasible and this work forms the basis for future systematic comparisons with newly developed post-processing algorithms and data assimilation techniques applied to the MRV data, preliminary results being presented in Egger and Teschner (2019). Ultimately, this study strives to improve in vivo measurements of the wall shear stress. One of the main challenges beyond those of the present study will be to accurately estimate the geometry of the pulsating vessel; hence, the wall position, since the wall shear stress estimate is extremely sensitive to knowing the wall-normal distance of the measured velocity.

Acknowledgements The authors would like to thank the German Research Foundation (DFG) for financially supporting this project under the Grants TR 194/56-1, HE 1875/30-1 and EG 331/1-1.

References

Amili O, Schiavazzi D, Moen S, Jagadeesan B, Van de Moortele PF, Coletti F (2018) Hemodynamics in a giant intracranial aneurysm characterized by in vitro 4d flow MRI. PloS One 13(1):e0188,323

Atherton TJ, Kerbyson DJ (1999) Size invariant circle detection. Image Vis Comput 17(11):795–803

Bauer A, Wegt S, Tropea C, Krafft A, Shokina N, Hennig J, Teschner G, Egger H (2018) Ground-truth for measuring wall shear stress with magnetic resonance velocimetry. In: 19th international symposium on the application of laser and imaging techniques to fluid mechanics

Berg P, Roloff C, Beuing O, Voss S, Sugiyama SI, Aristokleous N, Anayiotos AS, Ashton N, Revell A, Bressloff NW et al (2015) The computational fluid dynamics rupture challenge 2013-phase II: variability of hemodynamic simulations in two intracranial aneurysms. J Biomech Eng 137(12):121,008

Boussel L, Rayz V, McCulloch C, Martin A, Acevedo-Bolton G, Lawton M, Higashida R, Smith WS, Young WL, Saloner D (2008) Aneurysm growth occurs at region of low wall shear stress: patient-specific correlation of hemodynamics and growth in a longitudinal study. Stroke 39(11):2997–3002

Boussel L, Rayz V, Martin A, Acevedo-Bolton G, Lawton MT, Higashida R, Smith WS, Young WL, Saloner D (2009) Phase-contrast magnetic resonance imaging measurements in intracranial aneurysms in vivo of flow patterns, velocity fields, and wall shear stress: comparison with computational fluid dynamics. Magn Reson Med 61(2):409–417

Brenn G (2016) Analytical solutions for transport processes. Springer, New York

Bruschewski M, Schiffer HP, Grundmann S (2014) Measuring turbulent swirling flow with phase-contrast MRI. In: 17th international symposium on applications of laser techniques to fluid mechanics, Lisbon, Portugal

Bruschewski M, Freudenhammer D, Buchenberg WB, Schiffer HP, Grundmann S (2016) Estimation of the measurement uncertainty in magnetic resonance velocimetry based on statistical models. Exp Fluids 57(5):83

Budwig R, Elger D, Hooper H, Slippy J (1993) Steady flow in abdominal aortic aneurysm models. J Biomech Eng 115(4A):418–423. https://doi.org/10.1115/1.2895506

Bürk J, Blanke P, Stankovic Z, Barker A, Russe M, Geiger J, Frydrychowicz A, Langer M, Markl M (2012) Evaluation of 3d blood flow patterns and wall shear stress in the normal and dilated thoracic aorta using flow-sensitive 4d CMR. J Cardiovasc Magn Reson 14(1):84

Callaghan FM, Grieve SM (2018) Normal patterns of thoracic aortic wall shear stress measured using 4d-flow MRI in a large population. Am J Physiol Heart Circ Physiol 315:H1174–H1181

Caro CG (2012) The mechanics of the circulation. Cambridge University Press, Cambridge

Carpinlioglu MÖ, Gündogdu MY (2001) A critical review on pulsatile pipe flow studies directing towards future research topics. Flow Meas Instrument 12(3):163–174. https://doi.org/10.1016/s0955-5986(01)00020-6

Carvalho JL, Nielsen JF, Nayak KS (2010) Feasibility of in vivo measurement of carotid wall shear rate using spiral fourier velocity encoded MRI. Magn Reson Med 63(6):1537–1547

Clauser FH (1956) The turbulent boundary layer. Adv Appl Mech 4:1–51 (Elsevier)

D'Elia M, Perego M, Veneziani A (2012) A variational data assimilation procedure for the incompressible Navier–Stokes equations in hemodynamics. J Sci Comput 52(2):340–359. https://doi.org/10.1007/s10915-011-9547-6

Durst F, Ismailov M, Trimis D (1996a) Measurement of instantaneous flow rates in periodically operating injection systems. Exp Fluids 20:178–188. https://doi.org/10.1007/bf00190273

Durst F, Kikura H, Lekakis I, Jovanović J, Ye Q (1996b) Wall shear stress determination from near-wall mean velocity data in turbulent pipe and channel flows. Exp Fluids 20(6):417–428. https://doi.org/10.1007/bf00189380

Durst F, Müller R, Jovanovic J (2004) Determination of the measuring position in laser-doppler anemometry. Exp Fluids 6(2):105–110. https://doi.org/10.1007/bf00196460

Efstathopoulos EP, Patatoukas G, Pantos I, Benekos O, Katritsis D, Kelekis NL (2008) Wall shear stress calculation in ascending aorta using phase contrast magnetic resonance imaging. Investigating effective ways to calculate it in clinical practice. Phys Med Eur J Med Phys 24(4):175–181. https://doi.org/10.1016/j.ejmp.2008.01.004

Egger H, Teschner G (2019) On the stable estimation of flow geometry and wall shear stress from magnetic resonance images. Inverse Problems. https://doi.org/10.1088/1361-6420/ab23d5

Egger H, Seitz T, Tropea C (2017) Enhancement of flow measurements using fluid-dynamic constraints. J Comput Phys 344:558–574

El Khoury GK, Schlatter P, Noorani A, Fischer PF, Brethouwer G, Johansson AV (2013) Direct numerical simulation of turbulent

pipe flow at moderately high Reynolds numbers. Flow Turbulence Combust 91(3):475–495
Farag E, Vendrik J, van Ooij P, Poortvliet Q, van Kesteren F, Wollersheim L, Kaya A, Driessen A, Piek J, Koch K et al (2019) Transcatheter aortic valve replacement alters ascending aortic blood flow and wall shear stress patterns: a 4d flow MRI comparison with age-matched, elderly controls. Eur Radiol 29(3):1444–1451
Frydrychowicz A, Stalder AF, Russe MF, Bock J, Bauer S, Harloff A, Berger A, Langer M, Hennig J, Markl M (2009) Three-dimensional analysis of segmental wall shear stress in the aorta by flow-sensitive four-dimensional-MRI. J Magn Reson Imaging 30(1):77–84. https://doi.org/10.1002/jmri.21790
Ghil M, Malanotte-Rizzoli P (1991) Data assimilation in meteorology and oceanography. Adv Geophys 33:141–266 (Elsevier)
Glaßer S, Lawonn K, Hoffmann T, Skalej M, Preim B (2014) Combined visualization of wall thickness and wall shear stress for the evaluation of aneurysms. IEEE Trans Vis Comput Graph 20(12):2506–2515
Gronskis A, Heitz D, Mémin E (2013) Inflow and initial conditions for direct numerical simulation based on adjoint data assimilation. J Comput Phys 242:480–497
Gündogdu MY, Carpinlioglu MÖ (1999a) Present state of art on pulsatile flow theory: Part 1: Laminar and transitional flow regimes. JSME Int J Ser B Fluids Thermal Eng 42(3):384–397. https://doi.org/10.1299/jsmeb.42.384
Gündogdu MY, Carpinlioglu MÖ (1999b) Present state of art on pulsatile flow theory: Part 2: Turbulent flow regime. JSME Int J Ser B Fluids Thermal Eng 42(3):398–410. https://doi.org/10.1299/jsmeb.42.398
Harloff A, Nußbaumer A, Bauer S, Stalder AF, Frydrychowicz A, Weiller C, Hennig J, Markl M (2010) In vivo assessment of wall shear stress in the atherosclerotic aorta using flow-sensitive 4d MRI. Magn Reson Med 63(6):1529–1536. https://doi.org/10.1002/mrm.22383
Harloff A, Berg S, Barker A, Schöllhorn J, Schumacher M, Weiller C, Markl M (2013) Wall shear stress distribution at the carotid bifurcation: influence of eversion carotid endarterectomy. Eur Radiol 23(12):3361–3369. https://doi.org/10.1007/s00330-013-2953-4
Iguchi M, Ohmi M (1984) Transition to turbulence in a pulsatile pipe flow: 3rd report, flow regimes and the conditions describing the generation and decay of turbulence. Bull JSME 27(231):1873–1880. https://doi.org/10.1299/jsme1958.27.1873
Janiga G, Berg P, Sugiyama S, Kono K, Steinman D (2015) The computational fluid dynamics rupture challenge 2013-phase I: prediction of rupture status in intracranial aneurysms. Am J Neuroradiol 36(3):530–536
Kendall A, Koochesfahani M (2008) A method for estimating wall friction in turbulent wall-bounded flows. Exp Fluids 44(5):773–780
Kyomen S, Usui T, Fukawa M, Ohmi M (1996) Combined free and forced convection for laminar steady flow in horizontal tubes. JSME Int J Ser B Fluids Thermal Eng 39(1):44–50. https://doi.org/10.1299/jsmeb.39.44
Lambossy P (1952) Oscillations forcées d'un liquide incompressible et visqueux dans un tube rigide et horizontal: calcul de la force de frottement. Helvetica Phys Acta 25:371–386
Markl M, Wegent F, Zech T, Bauer S, Strecker C, Schumacher M, Weiller C, Hennig J, Harloff A (2010) In vivo wall shear stress distribution in the carotid artery: effect of bifurcation geometry, internal carotid artery stenosis, and recanalization therapy. Circ Cardiovasc Imaging 3(6):647–655
Markl M, Wallis W, Harloff A (2011) Reproducibility of flow and wall shear stress analysis using flow-sensitive four-dimensional MRI. J Magn Reson Imaging 33(4):988–994
Markl M, Frydrychowicz A, Kozerke S, Hope M, Wieben O (2012) 4d flow MRI. J Magn Reson Imaging 36(5):1015–1036. https://doi.org/10.1002/jmri.23632
Meng H, Wang Z, Hoi Y, Gao L, Metaxa E, Swartz DD, Kolega J (2007) Complex hemodynamics at the apex of an arterial bifurcation induces vascular remodeling resembling cerebral aneurysm initiation. Stroke 38(6):1924–1931
Musker A (1979) Explicit expression for the smooth wall velocity distribution in a turbulent boundary layer. AIAA J 17(6):655–657. https://doi.org/10.2514/3.61193
Otsu N (1979) A threshold selection method from gray-level histograms. IEEE Trans Syst Man Cybern 9(1):62–66. https://doi.org/10.1109/tsmc.1979.4310076
Paul EL, Atiemo-Obeng VA, Kresta SM (2004) Handbook of industrial mixing: science and practice. Wiley, New York
Peattie RA, Riehle TJ, Bluth EI (2004) Pulsatile flow in fusiform models of abdominal aortic aneurysms: flow fields, velocity patterns and flow-induced wall stresses. J Biomech Eng 126(4):438–446. https://doi.org/10.1115/1.1784478
Peiffer V, Sherwin SJ, Weinberg PD (2013) Does low and oscillatory wall shear stress correlate spatially with early atherosclerosis? A systematic review. Cardiovasc Res 99(2):242–250
Petersson S, Dyverfeldt P, Ebbers T (2012) Assessment of the accuracy of mri wall shear stress estimation using numerical simulations. J Magn Reson Imaging 36(1):128–138. https://doi.org/10.1002/jmri.23610
Piatti F, Pirola S, Bissell M, Nesteruk I, Sturla F, Della Corte A, Redaelli A, Votta E (2017a) Towards the improved quantification of in vivo abnormal wall shear stresses in bav-affected patients from 4d-flow imaging: benchmarking and application to real data. J Biomech 50:93–101
Piatti F, Sturla F, Bissell MM, Pirola S, Lombardi M, Nesteruk I, Della Corte A, Redaelli AC, Votta E (2017b) 4d flow analysis of bav-related fluid-dynamic alterations: evidences of wall shear stress alterations in absence of clinically-relevant aortic anatomical remodeling. Front Physiol 8:441
Potters WV, Ooij P, Marquering H, vanBavel E, Nederveen AJ (2015) Volumetric arterial wall shear stress calculation based on cine phase contrast MRI. J Magn Reson Imaging 41(2):505–516. https://doi.org/10.1002/jmri.24560
Ray S, Ünsal B, Durst F (2012) Development length of sinusoidally pulsating laminar pipe flows in moderate and high Reynolds number regimes. Int J Heat Fluid Flow 37:167–176
Rizk J, Latus H, Shehu N, Mkrtchyan N, Zimmermann J, Martinoff S, Ewert P, Hennemuth A, Stern H, Meierhofer C (2019) Elevated diastolic wall shear stress in regurgitant semilunar valvular lesions. J Magn Reson Imaging. https://doi.org/10.1002/jmri.26680
Rodríguez-López E, Bruce PJ, Buxton OR (2015) A robust post-processing method to determine skin friction in turbulent boundary layers from the velocity profile. Exp Fluids 56(4):68. https://doi.org/10.1007/s00348-015-1935-5
Salsac AV, Sparks S, Chomaz JM, Lasheras J (2006) Evolution of the wall shear stresses during the progressive enlargement of symmetric abdominal aortic aneurysms. J Fluid Mech 560:19–51. https://doi.org/10.1017/s002211200600036x
Schenck JF (1996) The role of magnetic susceptibility in magnetic resonance imaging: MRI magnetic compatibility of the first and second kinds. Med Phys 23(6):815–849
Schneiders JF, Scarano F (2016) Dense velocity reconstruction from tomographic PTV with material derivatives. Exp Fluids 57(9):139
Siedek F, Giese D, Weiss K, Ekdawi S, Brinkmann S, Schroeder W, Bruns C, Chang DH, Persigehl T, Maintz D et al (2018) 4d flow mri for the analysis of celiac trunk and mesenteric artery stenoses. Magn Reson Imaging 53:52–62
Steinman DA, Hoi Y, Fahy P, Morris L, Walsh MT, Aristokleous N, Anayiotos AS, Papaharilaou Y, Arzani A, Shadden SC et al (2013) Variability of computational fluid dynamics solutions for pressure and flow in a giant aneurysm: the ASME 2012 summer

bioengineering conference CFD challenge. J Biomech Eng 135(2):021,016
Szajer J, Ho-Shon K (2018) A comparison of 4d flow mri-derived wall shear stress with computational fluid dynamics methods for intracranial aneurysms and carotid bifurcations-a review. Magn Reson Imaging 48:62–69
Valen-Sendstad K, Bergersen AW, Shimogonya Y, Goubergrits L, Bruening J, Pallares J, Cito S, Piskin S, Pekkan K, Geers AJ et al (2018) Real-world variability in the prediction of intracranial aneurysm wall shear stress: the 2015 international aneurysm CFD challenge. Cardiovasc Eng Technol 9(4):544–564
Van Ooij P, Potters WV, Nederveen AJ, Allen BD, Collins J, Carr J, Malaisrie SC, Markl M, Barker AJ (2015) A methodology to detect abnormal relative wall shear stress on the full surface of the thoracic aorta using four-dimensional flow MRI. Magn Reson Med 73(3):1216–1227. https://doi.org/10.1002/mrm.25224
Van Ooij P, Markl M, Collins JD, Carr JC, Rigsby C, Bonow RO, Malaisrie SC, McCarthy PM, Fedak PW, Barker AJ (2017) Aortic valve stenosis alters expression of regional aortic wall shear stress: new insights from a 4-dimensional flow magnetic resonance imaging study of 571 subjects. J Am Heart Assoc 6(9):e005959
Vennemann P, Lindken R, Westerweel J (2007) In vivo whole-field blood velocity measurement techniques. Exp Fluids 42(4):495–511. https://doi.org/10.1007/s00348-007-0276-4
Womersley JR (1955) Method for the calculation of velocity, rate of flow and viscous drag in arteries when the pressure gradient is known. J Physiol 127:553–563. https://doi.org/10.1113/jphysiol.1955.sp005276
Xiang J, Natarajan SK, Tremmel M, Ma D, Mocco J, Hopkins LN, Siddiqui AH, Levy EI, Meng H (2011) Hemodynamic-morphologic discriminants for intracranial aneurysm rupture. Stroke 42(1):144–152
Yang Y, Cai S, Mémin E, Heitz D (2017) Ensemble-variational methods in data assimilation. In: 2nd Workshop on Data Assimilation & CFD Processing for Particle Image and Tracking Velocimetry

Affiliations

Andreas Bauer[1] · Sebastian Wegt[1] · Maximilian Bopp[1] · Suad Jakirlic[1] · Cameron Tropea[1] · Axel Joachim Krafft[2] · Nina Shokina[2] · Jürgen Hennig[2] · Gabriel Teschner[3] · Herbert Egger[3]

Andreas Bauer
bauer@sla.tu-darmstadt.de

[1] Institute of Fluid Mechanics and Aerodynamics, Technische Universität Darmstadt, Darmstadt, Germany

[2] Department of Radiology, Medical Physics, Medical Center, University of Freiburg, Freiburg, Germany

[3] Institute for Numerical Analysis and Scientific Computing, Technische Universität Darmstadt, Darmstadt, Germany